Assessing the potential of xNi-yMg-Al2O3 catalysts prepared by EISA-one-pot synthesis towards CO2 methanation: An overall study

Leila Karam, M. Carmen Bacariza, José David Lopes, Carlos Henriques, Pascale Massiani, Nissrine El Hassan

Assessing the potential of *x*Ni-*y*Mg-Al_2O_3 catalysts prepared by EISA-one-pot synthesis towards CO_2 methanation: An overall study

Leila Karam[a,b], M. Carmen Bacariza[c,*] José M. Lopes[c], Carlos Henriques[c], Pascale Massiani[a], Nissrine El Hassan[b,*]

[a] Sorbonne Université, UPMC Université Paris 06, CNRS-UMR 7197, Laboratoire de Réactivité de Surface, 4 Place Jussieu, Paris, France.

[b] University of Balamand, Faculty of Engineering, Department of Chemical Engineering, P.O. Box 33, Amioun El Koura, Lebanon.

[c] Centro de Química Estrutural, Instituto Superior Técnico, Universidade de Lisboa, Av. Rovisco Pais, 1049-001 Lisboa, Portugal.

*Corresponding authors: M. Carmen Bacariza: maria.rey@tecnico.ulisboa.pt; Nissrine El Hassan: nissrine.hassan@balamand.edu.lb

Abstract

Mesoporous *x*Ni-*y*Mg-Al_2O_3 catalysts prepared by combined evaporation induced self-assembly (EISA) and one-pot techniques were tested in CO_2 methanation reaction. All calcined/reduced materials were characterized by X-ray fluorescence (XRF), X-ray diffraction (XRD), N_2 physisorption, thermogravimetric analysis (TGA), CO_2 adsorption, H_2 temperature programmed reduction (H_2-TPR) and transmission electron microscopy (TEM). The effects of Mg and Ni loadings on the catalysts properties and performances were systematically studied. Higher Mg contents enhanced methanation performances due to more favourable metallic interactions between the Ni, Mg and Al species. In addition, higher Ni contents led to better selectivity to CH_4 by enhancing methane formation that involves H_2 dissociation on Ni^0 sites. The mesoporous 5Ni-Al_2O_3 catalyst obtained by the EISA-one-pot technique was significantly more active than silica-based catalysts with same 5 wt.% Ni content supported on USY zeolite and SBA-15. Moreover, the performances of the most promising 15Ni-7Mg-Al_2O_3 mesoporous material were similar to those of a commercial 25Ni/γ-Al_2O_3 catalyst in spite of its reduced nickel content.

Keywords: CO_2 methanation; Nickel; Magnesium; Alumina; EISA; One-pot.

1. Introduction

In order to face climate change, there is a worldwide concern to produce electricity from renewable sources. The intrinsic intermittency and unpredictability of some of them, like those issued from solar or wind technologies, strongly motivate the development of electric energy storage (EES) systems [1]. Among the different possibilities envisaged nowadays, the production of hydrogen from renewable energy produced in periods with low demand and its use to synthesize gases that can generate chemical energy (power-to-gas) is considered as a promising strategy [2,3]. In this way, power-to-methane which aims to produce CH_4 from CO_2 and renewable H_2, constitutes an appropriate strategy [4] with two important advantages. Firstly, it produces synthetic natural gas while simultaneously reducing CO_2 emissions, being hence especially relevant in context such as those of power or cement plants. Secondly, the produced synthetic natural gas can be integrated as such in the existing distribution grid without any need to implement new infrastructures.

CO_2 conversion into synthetic natural gas in presence of H_2, also known as CO_2 methanation, requires the use of a catalyst, whose composition and properties constitute one of the key aspects for the potential application of this reaction at a large scale. Amongst all methods and compositions tested to prepare active, selective and stable catalysts, alumina-based materials containing nickel have been widely studied due to the combination of the known durability and availability of alumina as adsorbing support and of the interest of nickel as hydrogenating metal phase able to substitute more expensive and rarer noble metals [5–7]. The main objective of the most recent studies published in this context dealt with the improvement of the dispersion of the nickel phase that shows high performances in this reaction but which drawback is to be highly sensitive to sintering [8]. Consequently, many preparation procedures were tested with the aim to increase the surface area of the alumina support and/or favour the nickel dispersion and stabilisation [9–16]. Conventional Ni/Al_2O_3 materials obtained by impregnation methods mainly led to relatively large Ni^0 particle sizes (10-30 nm) poorly attached on the support and favouring agglomeration processes during the course of the reaction [5,9]. Attempts have been done to synthesize the nickel-alumina-based materials by ultrasound assisted co-precipitation method [10], layered double hydroxide relying on plasma [11], microwave method with autoclave [12], partial hydrolysis of aqueous solution [13] and different alumina precursors [14]. However, many of these methods suffer from one or more deficiencies such as resulting in non-porous materials with low surface area, possible explosion during the preparation, expensive substrates or long-lasting synthesis procedures. Besides, the use of deposition-precipitation resulted in small particle sizes (e.g. 3.2 nm) but also to low activity (CO_2 conversion of 22%) due to deactivation during the test attributed to the oxidation of the most active Ni sites in the

presence of O_2 impurities [15]. The absence of organized porosity was also found to favour deactivation due to nickel sintering [9,10,15] or carbon deposition [12].

Amongst available synthesis procedures, the evaporation induced self-assembly (EISA) technique combined to a one-pot approach (direct addition of the metal in the synthesis gel) was recently found highly efficient for the preparation of ordered mesoporous nickel alumina catalysts showing excellent performances in CO_2 methanation [16,17]. Such method was also adopted to prepare nickel alumina catalysts highly stable in methane reforming reactions that involve harsh reaction conditions (high temperatures in the range 600-800°C, needed due to thermodynamic constraints) [18]. The advantage of this procedure is to enhance the interaction between the Ni metallic phase and the alumina support due to mixing the different components from the very first steps of preparation, favouring the extreme dispersion of the parent Ni^{2+} cations within the walls of the alumina matrix and its embedment in the form of nickel aluminate after calcination of the material [16–19]. In addition to the advantage of high durability of the Ni-Al_2O_3 system, this preparation method is moreover beneficial in terms of simplicity, highly favourable for potential application at an industrial scale, since the support preparation and nickel addition are carried out simultaneously, in a single step, avoiding the repetition of heating, recovery and purification sequences. This synthesis strategy was also extended for the addition to nickel, within the synthesis of the material, of a second metal such as cobalt [20], calcium [21] or rare earth metals (La, Ce, Sm, Pr) [22].

In addition, several studies on CO_2 methanation have revealed the possibility of enhancement of the performances by adding a basic additive [23–26] that increases the chemical adsorption of CO_2 and decreases in turn its activation energy. One of such additives is Mg (in the form of MgO) that has been shown to boost the support basicity, promote Ni dispersion and suppress sintering, limit carbon deposits formation and increase the performances of nickel based catalysts used in CO_2 methanation [27–29] and also other reactions involving the same gaseous molecules, namely reforming of methane with CO_2 carried out at significantly higher temperature [19,30,31]. In the continuation of this bibliographic knowledge, the objective of the present work was to benefit from the advantages of the EISA-one pot synthesis procedure to prepare Ni-Mg-Al_2O_3 catalysts with varying Ni and Mg contents and identify the effects of these contents on the physicochemical properties of the materials and their related performances in CO_2 methanation. Another purpose was also to systematically compare these materials to known silica-based or commercial catalysts. Such better understanding can indeed constitute a fruitful step towards optimization of the performances of this type of catalysts.

Therefore, a series of mesoporous *x*Ni-*y*Mg-Al_2O_3 materials with different Mg (0, 7 and 26 wt.% Mg for 5 wt.% Ni) and Ni (5, 10, 15 and 20 wt.% for 7 wt.% Mg) loadings was prepared by the EISA-one-pot technique. After their preparation, the calcined materials were characterized by complementary techniques including chemical analysis, XRD, N_2 sorption, TGA-DSC, CO_2 adsorption, H_2-TPR and TEM. They were then reduced and tested under CO_2 methanation conditions. Representative samples were compared with other types of catalysts already reported as promising for this reaction [32] and using either mesoporous (SBA-15) or organized microporous (USY zeolite) silica-based materials as supports. The performances of the best mesoporous alumina-based catalyst were also compared to those of a 25Ni/γ-Al_2O_3 commercial hydrogenation catalyst allowing asserting the efficiency of the EISA-one-pot synthesis route to prepared efficient methanation catalysts.

2. Material and methods

2.1. Chemicals

The chemicals used for the synthesis were pluronic P123 triblock copolymer ($EO_{20}PO_{70}EO_{20}$, M_n=5800, Sigma-Aldrich, 435465), Aluminum isopropoxide ($Al[OCH(CH_3)_2]_3$, M_n=204.24, Sigma-Aldrich, 220418), absolute ethanol (CH_3CH_2OH, M_n=46.07, Sigma-Aldrich, 64175), nickel nitrate hexahydrate ($Ni(NO_3)_2.6H_2O$, Mn=290.79, Sigma-Aldrich, 72253), magnesium nitrate hexahydrate ($Mg(NO_3)_2{\cdot}6H_2O$, M_n=256.41, Sigma-Aldrich, 203696) and 65 wt.% nitric acid (HNO_3, M_n=63.01, Johnson Matthey S.A). They were employed as received without additional purification.

2.2. Materials preparation

The mesoporous *x*Ni-*y*Mg-Al_2O_3 materials (where *x* and *y* represent the Ni and Mg wt.%, respectively) were synthesized using the developed one-pot evaporation induced self-assembly (EISA-one-pot) method established elsewhere [18,33]. A typical synthesis involved dissolving 1 g of P123 Pluronic triblock copolymer in 20 mL of absolute ethanol at ambient temperature (25 °C) under intense stirring. During the stirring process, 1.6 mL of HNO_3 was added simultaneously with A mmol of $Al[OCH(CH_3)_2]_3$, B mmol of $Ni(NO_3)_2.6H_2O$, and C mmol of $Mg(NO_3)_2{\cdot}6H_2O$ to the solution. The total Al+Ni+Mg molar composition was always kept constant and equal to 10 mmol (A+B+C = 10). Ni loading was varied between 5 to 20 wt.% and that of Mg was altered between 7 to 26 wt.%. The obtained mixture was covered with a polyethylene film (PE) and stirring was kept overnight to reach a complete dissolution of the chemicals added. Then, the solution was dried at 60 °C for 48 h to slowly evaporate ethanol and HNO_3 with the aid of a water circulator (Julabo) connected to two plastic tubes that circulate water to regulate and control the temperature. The resulted xerogels were calcined in a muffle furnace under air at 600 °C for 5 h with a heating rate of

0.5 °C·min^{-1} (thin bed conditions). For comparison purposes, three reference samples were prepared by incipient wetness impregnation. Two of them contain 5 wt.% Ni added on a prepared SBA-15 [32,34,35] or on a commercial USY zeolite (preparation conditions found in [36,37]). The third one is a commercial Ni/γ-Al_2O_3 sample with ~25 wt.% Ni and used for hydrogenation reactions. These three samples are denominated *5*Ni/USY, *5*Ni/SBA-15 and Commercial *25*Ni/γ-Al_2O_3, respectively.

2.3. Catalysts characterization

Nickel content was estimated by X-Ray Fluorescence (XRF) using a XEPOS spectrometer (Spectro Ametek). Quantitative data were obtained using the MicroPowder method combining the well-established fundamental parameters approach to XRF spectrometer calibration with automatic correction for matrix effects. Compton backscatter information was used from the sample to calculate the matrix interference. The obtained values can be seen in Table 1.

Thermogravimetric (TGA-DSC) analyses were performed on a Setsys Evolution TGA from Setaram instrument. All samples were saturated in water prior to the experiments. Then, a program was run by heating from room temperature till 400 ºC (heating rate of 10 ºC/min) under air flow (30 mL/min). Water molecules are mainly desorbed in this temperature range leading to an endothermic peak confirmed by DSC. The h index was deduced from the ratio of the mass losses at 150 °C (desorption of water molecules weakly interacting with the catalyst) and at 400 °C (desorption of all water molecules interacting with the catalyst). This calculated h index serves as a tool to measure and compare the strength of the water affinity (hydrophobicity) in the studied samples [38].

Powder X-Ray diffraction (XRD) measurements at wide angles were performed to determine the structural properties of the samples. The patterns were registered on a PANalytical XPert^3 diffractometer using a CuKα radiation and operating at a voltage of 30 KV, a current of 10 mA with 2θ range of 20° to 90°, time step of 2 s and λ equal to 1.5405 nm. To identify the crystalline phases in each sample, a standard powder XRD file was used (known as ICDD, International Center for Diffraction Data).

Textural properties were determined by N_2 adsorption-desorption isotherms recorded at -196 °C using an ASAP 2020 Micromeritics apparatus. The samples were degassed under vacuum for 2 h at 250 °C then the N_2-isotherm were plotted. Specific surface areas (SA) were calculated by the BET (Brunauer-Emmet-Teller) method applied at relative pressures between 0.05 and 0.25. Single point pore volumes (V_{total}) were obtained from the sorption branch at a relative pressure of 0.99. The t-plot method was moreover applied to determine the microporous volumes (V_{micro}) in the zeolitic sample.

Pore size distributions were calculated based on BJH (Barrett-Joyner-Halenda) formula applied to the desorption branch of the hysteresis loop.

CO_2 adsorption was carried out at 0 ºC on an Autosorb iQ equipment from Quantachrome. Before adsorption, the samples (~80 mg) were degassed under vacuum (1 h at 90 ºC and 4 h at 350 ºC).

H_2-TPR experiments were performed on a Micromeritics AutoChem II equipment. The catalysts (~100 mg) were firstly pre-treated at 250 °C under argon flow and then cooled down to the room temperature. After that, they were reduced under a 5%H_2/Ar flow, rising the temperature from the room temperature to 900 °C using a rate of 10 ºC/min. A TCD detector monitored the hydrogen consumed.

The evaluation of nickel nanoparticles average sizes and dispersion was performed by high-resolution transmission electron microscopy (HRTEM) examinations were done on a JEOL-JEM 200 electron microscope which operates at 200 keV (LaB_6 gun). Experimentally, the powders were suspended in ethanol for few minutes under ultrasound vibration and then deposited on a copper grid coated with a carbon membrane. The "*Comptage de Particules*" software available at LRS was used to estimate the average size of the nickel (Ni^0) particles. To do so, around 500 particles present in the grains were taken into consideration where the channels are oriented parallel to the electron beam.

2.4. Catalytic tests

Catalytic tests were carried out in a fixed-bed catalytic reactor at atmospheric pressure and using a constant catalyst mass (0.200 g). With the purpose of reducing Ni species into Ni^0, *in-situ* pre-reduction treatments were carried out under an 80%H_2/N_2 flow of 250 mL min^{-1} for 1 h at a temperature chosen according to H_2-TPR profiles (heating rate of 5 ºC min^{-1}) and equal to 800 ºC for the EISA-one-pot and commercial samples and 650 ºC and 700 °C for *5*Ni/SBA-15 and *5*Ni/USY, respectively. After cooling down to 250 °C, the reactants were introduced into the reactor at a molar ratio of H_2:CO_2:N_2 = 36:9:10 (total flow of 287 mL/min) and the CO_2 methanation reaction was performed at temperatures ranging from 250 to 450 ºC. Air Liquide supplied all gases, with purities ≥99.9990%. The reactor effluent was analysed using three Guardian® NG infrared detectors (Edinburgh Sensors) for CO_2, CH_4 and CO. Due to the variation of the number of moles in the Sabatier reaction, the outlet flow was controlled and variations were taken into account in the determination of the catalytic performances. Carbon balances were used to verify the presence of other carbon-based by-products in the effluent, where only CH_4 and CO were detected as products. CO_2 conversion rates (r) were determined by Equation 1, with $F_{CO2.inlet}$ ($mol_{CO2}.s^{-1}$) corresponding to the inlet molar flow of CO_2 and W (g) to the total mass of catalyst:

$$r\ (mol\ CO_2\ .s^{-1}.g^{-1}) = CO_2\ conversion \cdot\ F_{CO_2,inlet} \cdot\ (1/W) \qquad \text{(Equation 1)}$$

3. Results and discussion

3.1. Textural properties

Figure 1 shows the results of N_2 physisorption obtained for the series of calcined *x*Ni-*y*Mg-Al_2O_3 samples prepared by the EISA-one-pot method. All these materials exhibit a type IV isotherm with H1 hysteresis loop typical of mesoporous materials [39]. The hysteresis loop is steep for *5*Ni-Al_2O_3 and *5*Ni-*7*Mg-Al_2O_3 and followed by a plateau in the region of P/P_0 of 0.8-1 (Figure 1 a,b), which is characteristic of hexagonally ordered mesoporous structures [34,39]. The loop is thin and well defined, indicating a narrow pores distribution with mean pores size between 6 and 7 nm as also visualized on the BJH curves (inset in Figure 1). The total surface area (SA) and pores volumes (V_{total}) deduced from the isotherms are reported in Table 1. SA values are comparable for both samples (around 240 $m^2.g^{-1}$) but V_{total} is slightly higher in *5*Ni-*7*Mg-Al_2O_3 (0.56 $cm^3.g^{-1}$) than in *5*Ni-Al_2O_3 (0.50 $cm^3.g^{-1}$), in agreement with previous bibliographic reports indicating a better material ordering upon Mg addition [40]. The preservation of the shape of the isotherm when adding more nickel up to a certain level (*10*Ni-*7*Mg-Al_2O_3 and *15*Ni-7Mg-Al_2O_3, Figures 1 c,d) reveals that the EISA-one-pot synthesis strategy keeps efficient to produce high quality ordered mesoporous nickel-alumina materials with Ni content as high as 15 wt%. Nevertheless, at such loading, both the surface area and pores volume tend to decrease and the phenomenon is accentuated upon further nickel addition, leading to surface area and total pore volumes about 20% lower in *20*Ni-*7*Mg-Al_2O_3 than in *5*Ni-*7*Mg-Al_2O_3 (Table 1). Moreover, the isotherm of the nickel-richest *20*Ni-*7*Mg-Al_2O_3 sample reveals some loss of structural organization attested by a shrinkage and distortion of the loop (Figure 1 e). In addition to a possible restriction of N_2 accessibility to the pores due to the presence of more numerous and/or bigger nickel nanoparticles [34,39,41], it can be assumed that the higher amount of nickel nitrate precursor in the synthesis medium also perturbed the formation of the hexagonally orientated mesoporous alumina structure. Important textural changes similarly took place when a significant amount of Mg was added, resulting in a loss of steepness of loop of the isotherm, in its shifts to higher relative pressure, and in the absence of a plateau between P/P_0 of 0.8 (*5*Ni-*26*Mg-Al_2O_3, Figure 1 f). Then, the shape of the isotherm is typical of a poorly structured mesoporous material with occurrence of intergranular mesopores [39]. The pore size distribution and mean pore size are slightly enlarged compared to all other EISA-one-pot synthesized materials (insets in Figure 1).

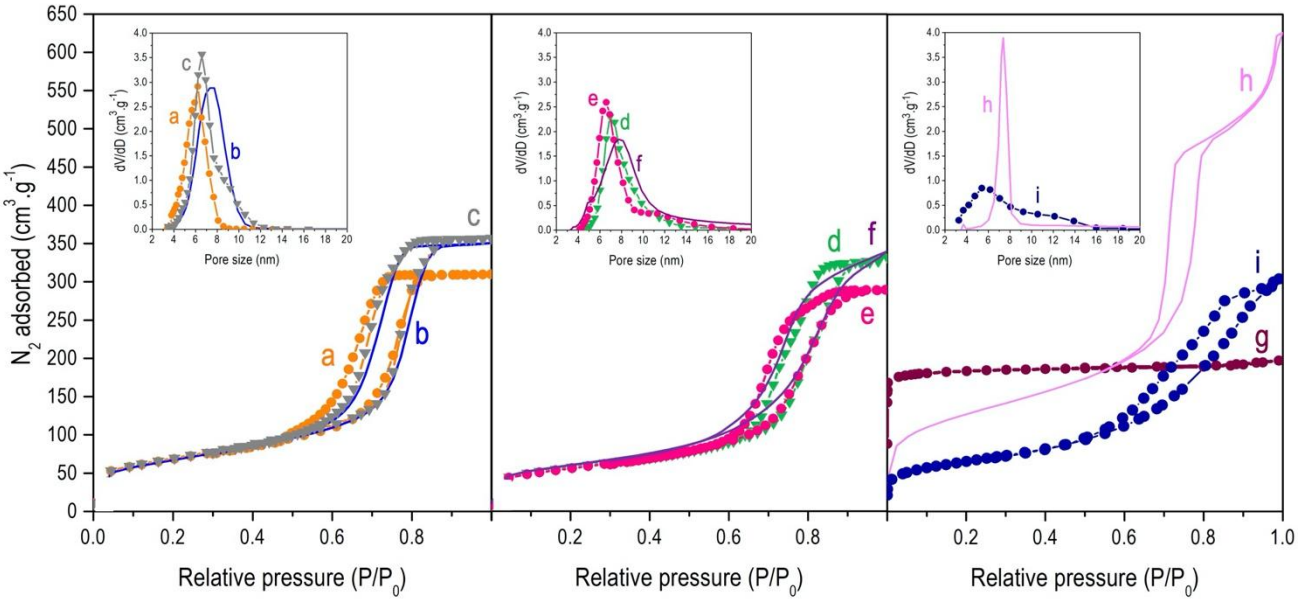

Figure 1. N_2 sorption isotherms and pore sizes distributions (in insets) of the calcined (a) *5*Ni-Al_2O_3, (b) *5*Ni-*7*Mg-Al_2O_3, (c) *10*Ni-*7*Mg-Al_2O_3, (d) *15*Ni-*7*Mg-Al_2O_3, (e) *20*Ni-*7*Mg-Al_2O_3 and (f) *5*Ni-*26*Mg-Al_2O_3 materials prepared by EISA-on-pot synthesis and (g) *5*Ni/USY, (h) *5*Ni/SBA-15 and (i) commercial *25*Ni/γ-Al_2O_3 reference samples.

Table 1. Physicochemical properties of the *x*Ni-*y*Mg-Al_2O_3 and reference samples.

Sample code	**Metal content (wt.%)**		**h index**[a]	$\mathbf{V_{total}}$[b] **(mL.g^{-1})**	**SA**[b] **(m^2.g^{-1})**	$\boldsymbol{d_{Ni^0}}$[c] **(nm)**	**D**[d] **(%)**
	Ni	Mg					
*5*Ni-Al_2O_3	4.8	0	0.55	0.50*(0.32)*	240*(173)*	4.6	21
*5*Ni-*7*Mg-Al_2O_3	4.7	7	0.45	0.56	240	4.5	21
*10*Ni-*7*Mg-Al_2O_3	9.4	7	0.41	0.57*(0.52)*	247*(219)*	5.9	17
*15*Ni-*7*Mg-Al_2O_3	14.1	7	0.46	0.54*(0.45)*	203*(160)*	6.4	16
*20*Ni-*7*Mg-Al_2O_3	19.4	7	0.45	0.47*(0.48)*	197*(198)*	9.0	11
*5*Ni-*26*Mg-Al_2O_3	5.0	26	0.38	0.54	205	8.8	11
*5*Ni/SBA-15	5.0	-	0.98	0.57	454	8.5	12
*5*Ni/USY	5.0	-	0.52	0.32*	581	23.0	4
*25*Ni/γ-Al_2O_3	~25	-	0.77	0.45*(0.42)*	229*(103)*	12.0	9

a: h index deduced from TGA-DSC of calcined samples

b: total pore volumes (V_{total}) and surface area (SA) evaluated from N_2 sorption isotherms of calcined and *(reduced)* samples; *the volume in the zeolitic sample is mainly microporous (V_{micro}=0.28 mL.g^{-1}) while it concerns mesopores in all other samples.

c: average Ni^0 particles sizes values estimated from the histograms obtained from representative TEM micrographs of each reduced sample;

d: Ni^0 nanoparticles dispersion calculated from TEM of reduced samples

For the sake of comparison, Figure 1 also shows the isotherms of the reference samples. In line with the well-known of the hexagonally ordered mesopores in SBA-15 [42], *5*Ni/SBA-15 displays a type IV isotherm with an H1 hysteresis loop (Figure 1 h) analogous to those observed above for the Ni poorer *x*Ni-*7*Mg-Al_2O_3 samples. A similarity between this reference silica-based sample and the EISA-one-pot synthesized alumina materials also exists with respect to their total pore volume, but

the surface area of *5*Ni/SBA-15 reaches a higher value of 450 $m^2.g^{-1}$, in accordance with the literature (Table 1) [42]. As expected, mesopores are no longer detected in the zeolitic *5*Ni/USY sample that shows a type I isotherm with important N_2 adsorption at very low relative pressure, characteristic of a material with almost exclusively micropores (Figure 1 g). Finally, commercial *25*Ni/γ-Al_2O_3 exposes an isotherm that reveals a disordered structure of Al_2O_3 support with random pores (Figure 1 i).

3.2. Surface properties

Starting with the evaluation of the catalysts interaction with water (a reaction product that is known to have an eventual inhibitory role in the methanation reaction [43,44], TGA-DSC experiments were carried out in the 25 to 400 ºC temperature range (10 ºC/min) on selected samples, after their saturation with adsorbed water, for determining their h indexes (Table 1). As mentioned in section 2.3, the h index (ratio between the mass losses at 150 and 400 ºC, respectively) gives an indication of the strength of water interaction with the samples, h indexes close to 1 being representative of hydrophobic materials while lower values suggest a stronger interaction between water molecules and the material [38]). As shown in Table 1, increasing the Mg loading strengthens the hydrophilicity (lower h indexes) what can eventually result in a higher water concentration over the catalysts during the reaction and thus in a higher inhibitory effect. The values in Table 1 also reveal that there is no remarkable effect of the Ni content on the h index, suggesting that the water inhibitory effect will be similar whatever the Ni content from 5 to 20 wt.%. Regarding the comparison with the silica-based reference materials, *5*Ni/SBA-15 presents a much lower interaction with water (h index of 0.98) while that in *5*Ni/USY is similar to those of the EISA-one-pot samples, involving potentially in this case hydration of the charge zeolitic framework compensating cations. Also, the interaction between water and the *25*Ni/γ-Al_2O_3 commercial catalyst is weaker than for the mesoporous samples of the *x*Ni-*y*Mg-Al_2O_3 series, indicating again a probable lower inhibitory role of water during reaction over this sample.

The surface properties were also analysed by collecting CO_2 adsorption isotherms (Figure 2). This technique was adopted to compare the affinity of the samples towards CO_2 that is present as a reactant during the methanation reaction. Starting with the samples with 5 wt.% Ni and different wt.% Mg (Figure 2 a,b,f), all samples present comparable CO_2 uptakes at high pressures. Nevertheless, in terms of affinity (low relative pressure points), the *5*Ni-*26*Mg-Al_2O_3 sample shows significantly enhanced CO_2 uptakes, confirming the stronger CO_2 interaction expected when more Mg (in the form of MgO) and hence higher basicity is present. Regarding the samples prepared with different Ni loadings (Figure 2 b-e), the affinity to CO_2 varied as follows: *5*Ni-*7*Mg-Al_2O_3 >> *10*Ni-

*7*Mg-Al_2O_3 ≅ *15*Ni-*7*Mg-Al_2O_3≅ *20*Ni-*7*Mg-Al_2O_3. The effect of Mg in facilitating CO_2 adsorption therefore appears to be higher at low Ni loading, while higher Ni loadings would reduce the benefits of Mg incorporation, possibly because of some limitation in the accessibility to the adsorption sites. Comparison with the other materials (Figure 2 g-i) reveals firstly a CO_2 uptake for *5*Ni/SBA-15 close to that of EISA-one-pot mesoporous *5*Ni-Al_2O_3 at P/P_0 of 0.03, but the shape of the curve at low pressure suggests a stronger interaction of CO_2 with the silica-based sample. Secondly, the affinity of CO_2 with *5*Ni/USY is much higher (especially at low P/P_0), probably due to the interaction of carbon dioxide with the compensating cations present in the pores [45]. Finally, the behaviour of the commercial sample is similar to that of *15*Ni-*7*Mg-Al_2O_3 sample. However, while its affinity to CO_2 is slightly higher than for the EISA-one-pot synthesized sample at low P/P_0 of CO_2, this tendency is inversed at higher relative pressures.

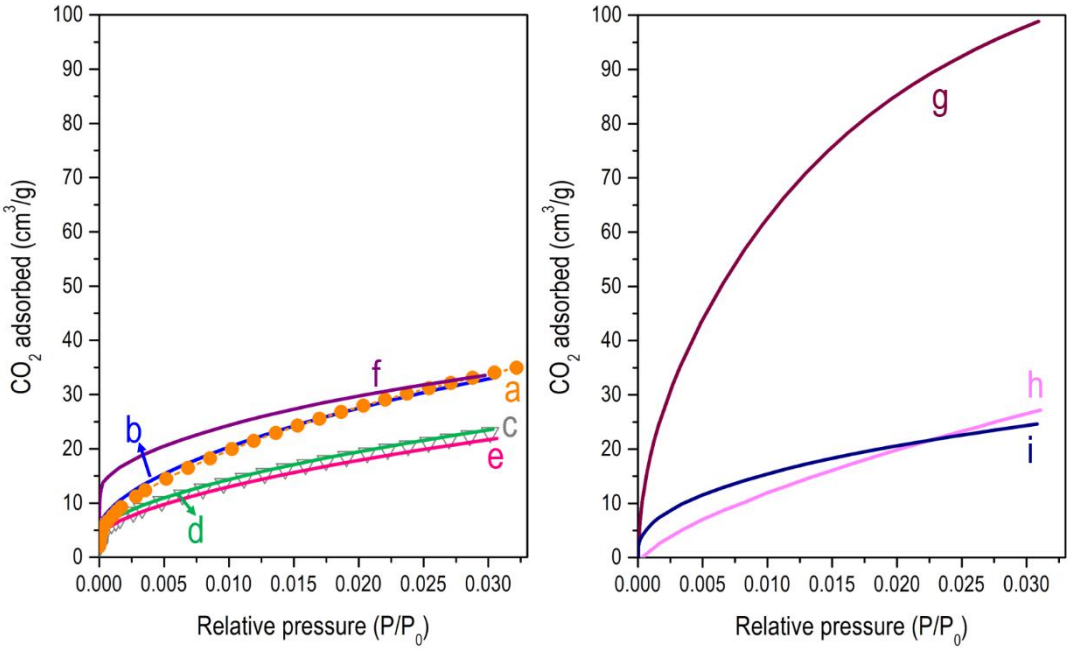

Figure 2. CO_2 isotherms for the calcined (a) *5*Ni-Al_2O_3, (b) *5*Ni-*7*Mg-Al_2O_3, (c) *10*Ni-*7*Mg-Al_2O_3, (d) *15*Ni-*7*Mg-Al_2O_3, (e) *20*Ni-*7*Mg-Al_2O_3 and (f) *5*Ni-*26*Mg-Al_2O_3 materials prepared by EISA-on-pot synthesis and (g) *5*Ni/USY, (h) *5*Ni/SBA-15 and (i) commercial *25*Ni/γ-Al_2O_3 reference samples.

3.3. Nickel reducibility

As indicated by H_2-TPR profiles (Figure 3), all the catalysts prepared by the EISA-one-pot method show a unique reduction peak at temperatures higher than 600 °C, independently of the amount of magnesium or nickel added. This indicates the absence of free NiO species (typically reduced at 300-400 ºC) and the presence of exclusively Ni species strongly interacting with the organized alumina support. The reduction peak for the un-promoted *5*Ni-Al_2O_3 sample (Figure 3 a) occurring at ~770 ºC is assignable to the reduction of Ni ions in an aluminate phase [46–48], normally occurring at

~800 ºC but probably shifted towards lower temperatures due to the low Ni content. When incorporating 7 wt.% Mg (Figure 3 b), the Ni species reduction occurs at ~700 ºC and the reduction peak is broader, suggesting the presence of new interactions of different strengths between Ni and Mg. For the samples with the same Mg loading (7 wt.%, Figure 3 b-e), again a unique reduction peak is observed in the 600-800 °C range, asserting on the strong metal support interaction even with high Ni loadings. Nevertheless, increasing the nickel content leads to a shift of the maximum of the peak towards higher temperatures, a behaviour that suggests a presence of Ni as $NiAl_2O_4$ [47,48], in addition to the availability of more nickel that retards the reduction of the samples and appearance of the maximum peak at a later temperature in a dynamic TPR process. It is important to mention that for the aforementioned samples, the H_2-uptake is in agreement with the Ni percentage present in each sample, with an amount of H_2 consumed of 800 μmol.g^{-1} for *5*Ni-*7*Mg-Al_2O_3 (corresponding to 5 wt.% Ni), 1600 μmol.g^{-1} for *10*Ni-*7*Mg-Al_2O_3 (corresponding to 9 wt.% Ni), 2400 μmol.g^{-1} for *15*Ni-*7*Mg-Al_2O_3 (corresponding to 14 w.% Ni) and 3300 μmol.g^{-1} for *20*Ni-*7*Mg-Al_2O_3 (corresponding to 19 wt.% Ni).

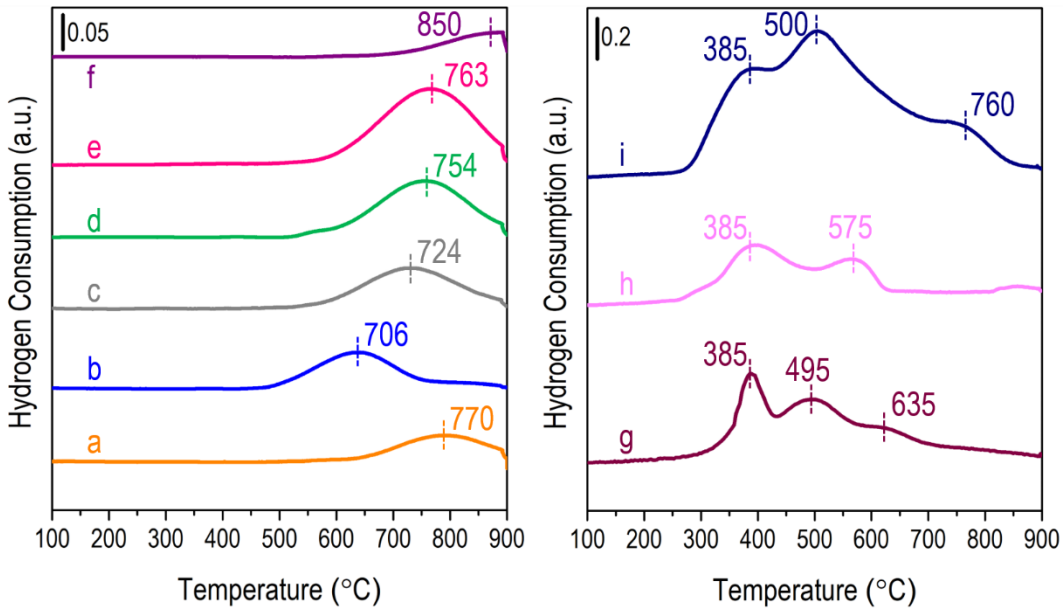

Figure 3. H_2-TPR profiles for the calcined (a) *5*Ni-Al_2O_3, (b) *5*Ni-*7*Mg-Al_2O_3, (c) *10*Ni-*7*Mg-Al_2O_3, (d) *15*Ni-*7*Mg-Al_2O_3, (e) *20*Ni-*7*Mg-Al_2O_3 and (f) *5*Ni-*26*Mg-Al_2O_3 materials prepared by EISA-on-pot synthesis and (g) *5*Ni/USY, (h) *5*Ni/SBA-15 and (i) commercial *25*Ni/γ-Al_2O_3 reference samples.

A high reduction temperature is also observed when fixing the amount of Ni to 5 wt.% and increasing the Mg content to 26 wt.% (Figure 3 f), and its maximum is unusually positioned above 800 °C, revealing a strengthening of the interaction between Ni and its environment, probably due to the formation of a highly stable solid NiO-MgO solution, whose characteristic diffraction peaks will

be confirmed below (see section 3.4). This agrees with previous observations of the formation of $NiMgAl_2O_4$ species in Mg-rich nickel alumina materials [48,49].

By comparison, the temperatures of reduction are systematically lower with the three reference materials (Figure 3 g-i), illustrating the strong effects of the type of support and Ni incorporation method on the nature of the metal species and strength of the metal-support interactions. Thus, several reduction peaks are systematically detected for all reference catalysts. For *5*Ni/SBA-15, the two main reduction peaks are positioned at ~400 and ~550 ºC, which is typical of NiO species weakly and strongly interacting with the mesoporous silica support, respectively [32,35,50]. For *5*Ni/USY, they are centred at ~320 ºC and 400 ºC and are hence assignable to the reduction of NiO particles deposited on the zeolite external surface and to Ni^{2+}/NiO species located in the zeolite supercages, respectively [36,51,52]. Additional reduction processes also happen at temperatures above 600 ºC, being attributed to the reduction of Ni^{2+} species ion-exchanged in the zeolite solid cages and hexagonal prisms [36,51,52]. Finally, *25*Ni/γ-Al_2O_3 exhibits two reduction peaks indicative of (i) NiO species weakly interacting with the alumina support (~450 ºC) and (ii) NiO (500-600 ºC) and/or Ni aluminate species (700-800 ºC) species strongly interacting with the support.

3.4. Crystallinity of materials and metal phases identification

Figure 4 reports the X-Ray diffraction patterns of the materials prepared by the EISA-one-pot method. For both *5*Ni-Al_2O_3 and *5*Ni-*7*Mg-Al_2O_3 having limited Ni and Mg contents, no diffraction peak is detected (Figure 4 a,b). This reveals, firstly, that the alumina walls of the support itself are amorphous and, secondly, that the Ni-based species (and Mg-based ones for *5*Ni-*7*Mg-Al_2O_3) are either amorphous or highly dispersed within the alumina in the form of nanospecies with sizes below the detection limit of XRD. Reaching 15 wt.% Ni (*15*Ni-*7*Mg-Al_2O_3), new diffraction peaks appear at different diffraction angles (2θ = 37°, 43° and 63.5°) and they are more intense in the case of *20*Ni-*7*Mg-Al_2O_3 (Figure 4 d,e). These peaks are broad and not fully symmetrical, revealing a possible simultaneous presence of two types of species (NiO and $NiAl_2O_4$) and a disturbed repartition of Ni particles in response to the higher Ni loading. In the Mg-rich *5*Ni-*26*Mg-Al_2O_3 material (Figure 4 f), no crystalline Ni is observed but the strong increase of the Mg loading triggers the appearance of new peaks at 2θ equal to 37°, 43°, 63°, 75° and 78° assignable to the (111), (200), (220), (311) and (222) reticular plans of crystalline MgO, respectively (JCPDS: 78-0430).

The absence of peaks - or the presence of only tiny ones - in most samples (expect Mg-rich *5*Ni-*26*Mg-Al_2O_3) strongly contrasts with the distinct intense XRD peaks typical of NiO exhibited by all three calcined references *5*Ni/USY, *5*Ni/SBA-15 and *5*Ni-Al_2O_3, whatever the nature or pores system

of the support (symbol o, **Supporting information Figure S1**). The detection of crystalline NiO in both SBA-15 and USY silica-based materials in spite of their limited Ni content (5 wt.%) suggests a much lower Ni dispersion, and hence larger particles, than in the mesoporous *5*Ni-Al_2O_3 prepared by the EISA-one-pot method. Additionally, in the case of *5*Ni/USY the characteristic peaks of faujasite (FAU) structure can be verified at 2θ equal to 6, 10, 16, 9, 20, 24, 27 and 31º [53], indicating that the zeolite structure was preserved after Ni incorporation.

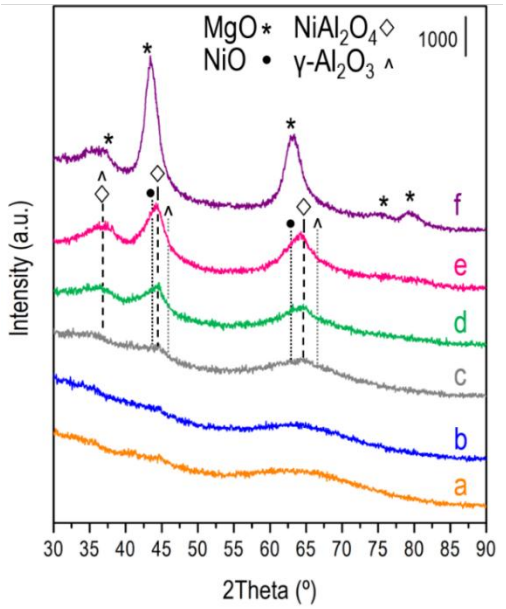

Figure 4. XRD diffractograms of calcined (a) *5*Ni-Al_2O_3, (b) *5*Ni-*7*Mg-Al_2O_3, (c) *10*Ni-*7*Mg-Al_2O_3, (d) *15*Ni-*7*Mg-Al_2O_3, (e) *20*Ni-*7*Mg-Al_2O_3 and (f) *5*Ni-*26*Mg-Al_2O_3 materials synthesized by EISA-one-pot method.

3.5. Morphologies of the alumina grains and Ni repartition in the reduced catalysts

After reduction of the catalysts, TEM images were recorded (Figure 5) to visualize the location of the Ni^0 particles on the alumina support and estimate their average sizes (Table 1). A high and homogeneous Ni dispersion is thus verified in *5*Ni-Al_2O_3 (Figure 5A) with an average particle size of 4.6 nm. Also, the parallel ordered channels of the alumina walls clearly appear, in good agreement with the N_2 physisorption results. The incorporation of 7 wt.% Mg (Figure 5B) preserves the Ni^0 dispersion (mean nickel particle size of 4.5 nm) and the mesoporosity of the alumina support. Also, in accordance with the collected isotherms (Figure 1), the TEM picture of *5*Ni-*26*Mg-Al_2O_3 (Figure 5C) proves that an excessive Mg loading destroys the parallel channel of the alumina, leading to a porous material of ill-defined morphology. The average Ni^0 particle size in this sample is higher (8.8 nm), stressing out the poorer nickel distribution. Furthermore, for the reduced mesoporous *x*Ni-*y*Mg-Al_2O_3 catalysts, the TEM pictures and physisorption curves are again in accordance, showing a global preservation of the structure after the reduction temperature treatment of 800 °C, except for a small decrease in surface area and pore volume values (Table 1) due to some thermally induced

shrinkage of the alumina walls. Simultaneously, the nickel faces a progressive agglomeration in the *x*Ni-*7*Mg-Al_2O_3 series of reduced catalysts when augmenting the nickel loading from 5, 10, 15 to 20 wt.%, the mean Ni^0 nanoparticles sizes indeed increasing from 4.5 to 5.9 then 6.4 and finally 9.0 nm, respectively (Figures 5 B, C, D, E, F and Table 1). Despite this decline in metal dispersion with higher Ni loading, the method of preparation of the mesoporous Ni-$MgAl_2O_3$ materials contributes to the formation of nanoparticles that are systematically much smaller than those identified in reduced *5*Ni/SBA-15 (Figure 5G), *5*Ni/USY (Figure 5H) and *25*Ni/γ-Al_2O_3 (Figure 5I), even at high Ni amount. Thus, the mean Ni^0 particle sizes are as high as 8.5 and 23 nm in *5*Ni/SBA-15 and *5*Ni/USY, respectively (i.e. about 47% and 80% larger than in *5*Ni-Al_2O_3 and *5*Ni-*7*Mg-Al_2O_3 with same 5 wt.% Ni content) and the commercial *25*Ni/γ-Al_2O_3 sample (Figure 5I) containing 25 wt.% Ni possesses Ni^0 nanoparticles of 12 nm in size, about 20% larger than in *20*Ni-*7*Mg-Al_2O_3 (see Table 1).

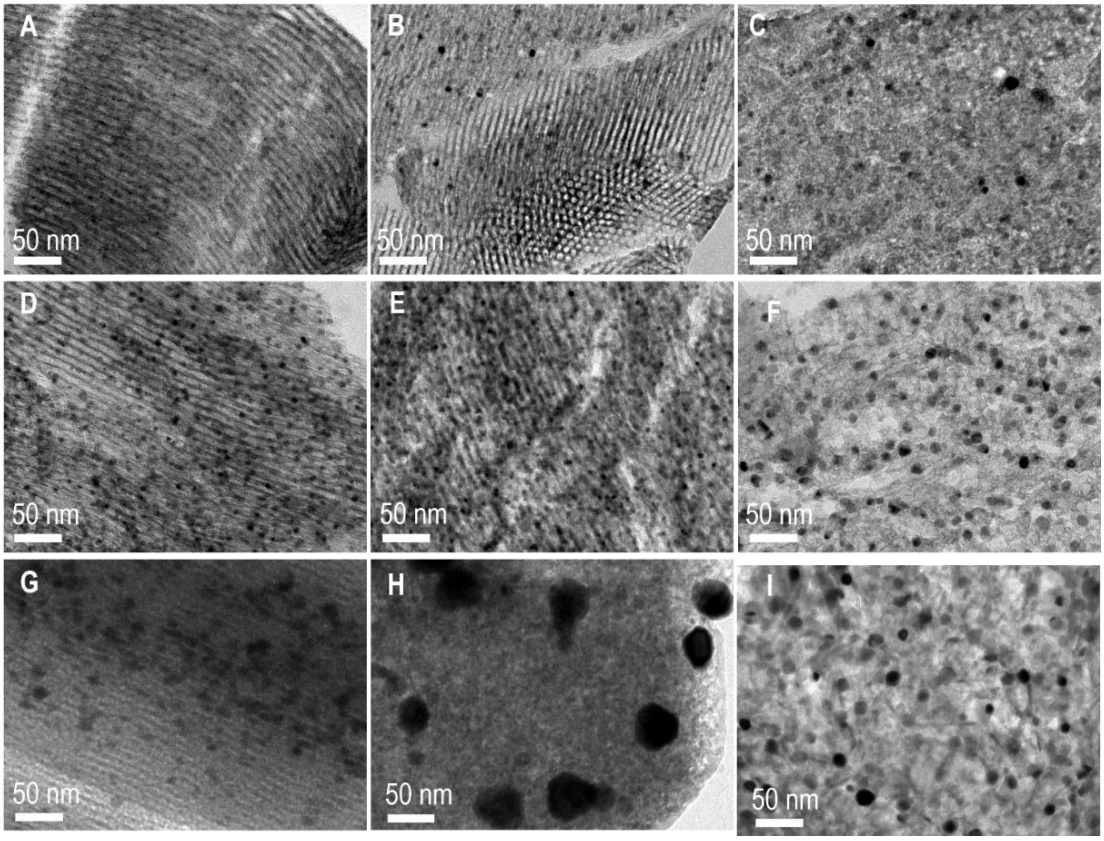

Figure 5. TEM micrographs collected after pre-reduction treatment for samples (A) *5*Ni-Al_2O_3, (B) *5*Ni-*7*Mg-Al_2O_3, (C) *5*Ni-*26*Mg-$Al_2O_3$10, (D) *10*Ni-*7*Mg-Al_2O_3, (E) *15*Ni-*7*Mg-Al_2O_3, (F) *20*Ni-*7*Mg-Al_2O_3, (G) *5*Ni/SBA-15, (H) *5*Ni/USY and (I) Commercial *25*Ni/γ-Al_2O_3.

3.6. Catalytic performances towards CO_2 methanation

The performances of all reduced catalysts were evaluated in CO_2 methanation. Figure 6 reports the evolutions of the CO_2 conversion (Figure 6A) and selectivity to CH_4 as a function of temperature

(Figure 6B). As usually observed for this reaction, the CO_2 conversions increase with temperature, till reaching a plateau and then tending to decrease for the most performing materials because of approaching the thermodynamic equilibrium (dotted line in Figure 6A). For the sake of completion, the CH_4 yields and reaction rates that follow the same trends are also provided (**Supporting information S2**).

Prior to data analysis, it can be recalled that on Pd-Mg/SiO_2 catalysts, Park *et al.* [27,54] proposed that CO_2 methanation occurs according to a bifunctional mechanism in which the magnesium-containing oxide stabilizes the adsorbed CO_2 molecules as surface carbonates that are subsequently hydrogenated by hydrogen atoms produced from H_2 dissociation on metal (Pd) sites. Such bifunctional mechanism was also reported by Cárdenas-Arenas *et al.* [55] over monometallic Ni-Al_2O_3, involving the alumina support (for CO_2 adsorption/activation) and Ni^0 (for catalytic H_2 dissociation). This process is similarly expected on the all series of *x*Ni-*y*Mg-Al_2O_3 catalysts prepared by EISA-one-pot synthesis route and it agrees with the catalytic results presented below.

Firstly, the Mg incorporation into the *5*Ni-Al_2O_3 catalyst systematically induced an increase in the CO_2 conversion (Figure 6A a,b,f). Taking into account that the nickel dispersions are comparable in both *5*Ni-Al_2O_3 and *5*Ni-*7*Mg-Al_2O_3 catalysts (with same Ni content), the beneficial effect of Mg can be unambiguously ascribed to the promotion of the CO_2 adsorption/activation over the more basic Mg-enriched alumina support [27–29]. Such effect was similarly reported after addition of Ca into Ni-Al composite oxide methanation catalysts [21]. The promoting effect of Mg still exists in the catalyst with 26 wt.% Mg (Figure 6A f), but the gain is then limited compared to *5*Ni-*7*Mg-Al_2O_3 (Figure 6A b), due the lower Ni dispersion, less ordered mesoporous network and higher inhibiting effect of water (lower h index) in the Mg-rich catalyst (Table 1). Besides, on these catalysts with 5 wt.% Ni, the CH_4 selectivity is above 90% at low temperature, but it then decreases and increases again, giving a minimum at ~325 ºC. Based on an *Operando* FTIR study, such behavior was earlier explained by an accumulation of adsorbed CO species on the catalyst surface between 300 to 350 ºC, limiting its dissociation/hydrogenation [56].

Secondly, the involvement of the metal function in activating the H_2 dissociation into H atoms [27,32,57–60] is confirmed by the progressive CO_2 conversion enhancement when increasing the Ni amount (while keeping the Mg content at 7 wt.%, Figure 6A b-e). The increase in conversion is however not totally proportional to the Ni content in the *x*Ni-*7*Mg-Al_2O_3 catalysts. Particularly, when moving from *15*Ni-*7*Mg-Al_2O_3 to *20*Ni-*7*Mg-Al_2O_3 (with about 30% more Ni), the conversion increases by only a few % (Figure 6A e,f). This is easily explained by the simultaneous decrease by c.a. 30% of the nickel dispersion (Table 1), reducing in turn the number of active sites for H_2

dissociation. It is also worth recalling that the samples with Ni loadings above 5 wt.%, have a lower CO_2 adsorption capacity (section 3.2), which could slightly reduce as well the positive effect of adding more Ni. In spite of these limitations, a clear additional benefit of increasing the Ni loading is to promote the selectivity to methane that keeps very high (between 96 and 99%), whatever the temperature of reaction (Figure 6B d-f). In a recent DRIFT study, it was proposed that high Ni loadings promote the selectivity to methane by facilitating the hydrogenation of the adsorbed formate and methyl intermediates [41].

A further important aspect to mention is the high catalytic stability of the mesoporous EISA-one-pot *x*Ni-*y*Mg-Al_2O_3 catalysts. This is illustrated in Figure 6C taking as representative examples the *5*Ni-*7*Mg-Al_2O_3 (curves b) and *15*Ni-*7*Mg-Al_2O_3 (curves d) catalysts that were tested at 350 °C for 10 h (as well as for 20 h for *15*Ni-*7*Mg-Al_2O_3 catalyst, Figure S3 – Supporting Information) and did not show any deactivation phenomenon, both activity and selectivity being kept unchanged during the all test duration, independently of the catalyst efficiency.

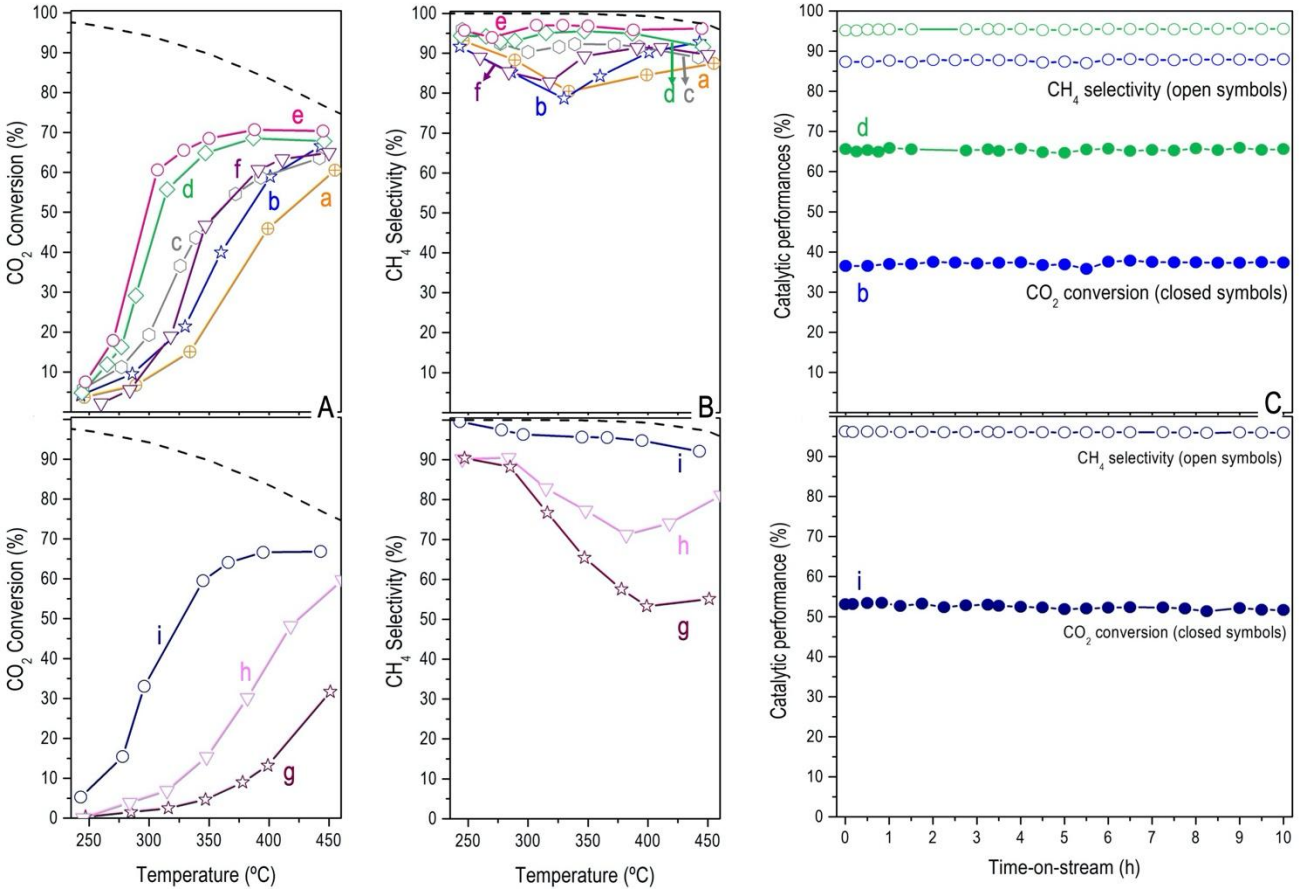

Figure 6. Evolution with temperature of the (A) CO_2 conversion and (B) CH_4 selectivity on the reduced (a) *5*Ni-Al_2O_3, (b) *5*Ni-*7*Mg-Al_2O_3, (c) *10*Ni-*7*Mg-Al_2O_3, (d) *15*Ni-*7*Mg-Al_2O_3, (e) *20*Ni-*7*Mg-Al_2O_3 and (f) *5*Ni-*26*Mg-Al_2O_3 EISA-one-pot catalysts and (g) *5*Ni/USY, (h) *5*Ni/SBA-15 and (i) commercial *25*Ni/γ-Al_2O_3 reference catalysts. (C) CO_2 conversion and CH_4 selectivity during stability test carried out for 10 h at 350 ºC. Dashed lines represent thermodynamic equilibrium conversions and selectivity determined with the Aspen Plus® software.

Moreover, when comparing the three prepared Mg-free 5 wt.% Ni catalysts (Figure 6 a,g,h), the performances follow the order: *5*Ni-Al_2O_3 > *5*Ni/SBA-15 >> *5*Ni/USY. The comparison is more clear when drawing the three curves together as is presented with yields of methane in the Supporting Information (**Figure S2** a,h,g). The better results exhibited by the EISA-one-pot synthesized material agrees again with its significantly higher metallic dispersion (Table 1). By increasing the number of metal surface sites, the latter is also favorable to methane selectivity which is between 76% and 90% on *5*Ni-Al_2O_3 (Figure 6B b) but decreases down to 70% or even 55% on *5*Ni/SBA-15 and *5*Ni/USY, respectively (Figure 6B h,g). Turning now to the Ni-rich catalysts, both the *15*Ni-7Mg-Al_2O_3 and commercial *25*Ni/γ-Al_2O_3 give similar CH_4 yields in spite of the lower metal content in the former catalyst (**Figure S2** d,i).

Above data demonstrate that the EISA-one-pot synthesis is a simple and efficient route of preparation of mesoporous *x*Ni-*y*Mg-Al_2O_3 catalysts for CO_2 methanation. Up to a 15 wt.% Ni and 7 wt.% Mg contents, the material is structurally ordered and the elemental dispersions (Ni and Mg) are high and homogeneous, *15*Ni-*7*Mg-Al_2O_3 being thus the most efficient of the prepared series of catalysts. Finally, for the sake of completion, we attempted to compare its performances to those of nickel-oxide catalysts reported in the literature. Due to variable contact times and reaction temperatures conditions used for the reaction, we determined CO_2 conversion rates (as defined in section 2.4) for CO_2 conversions not too close to equilibrium from available data for the catalysts detailed in Table 2. Figure 7 shows the obtained rates as a function of the reaction temperature. From this comparison, the *15*Ni-*7*Mg-Al_2O_3 catalysts is amongst the best alumina-based catalysts and it is better than the 20Ni-Al_2O_3 catalyst prepared by impregnation (curve (e), Figure 7). The conversions rates are higher for the samples supported on zirconia (curves (f) and (g), Figure 7) that is however more expensive and less abundant than alumina. The Ni sponge catalyst is also very active due to its fully metallic composition. Finally, it has to be highlighted that the same trends can be observed when comparing the CO_2 conversion rates obtained for all the catalysts presented in Figure 7 for a CO_2 conversion of 20% (Figure S4 – Supporting information).

Table 2. Conditions of tests and formulations of the catalysts taken from bibliography and compared in Figure 7, in term of CO_2 conversion rates (as defined in section 2.4), to the best mesoporous *15*Ni-*7*Mg-Al_2O_3 catalyst prepared in this work. All catalysts were tested at atmospheric pressure, using a H_2:CO_2 ratio of 4:1.

Catalysts formulation[a]	**Preparation method**	**P_{CO2}** [c] **(bar)**	**W** [d] **(g)**	**$F_{CO2\ inlet}$** [e] **(mol/s)**	**Ref.**
15Ni-7Mg-Al_2O_3	EISA-one-pot	0.16	0.200	$3.21 \cdot 10^{-5}$	This work
(a) 10Ni-Al_2O_3	EISA-one-pot	0.20	0.100	$3.41 \cdot 10^{-6}$	[17]
(b) 10Ni-8Ca-Al_2O_3	EISA-one-pot	0.20	0.100	$3.41 \cdot 10^{-6}$	[21]
(c) 10Ni-3Pr-Al_2O_3	EISA-one-pot	0.20	0.100	$3.41 \cdot 10^{-6}$	[22]
(d) 10Ni-1Ru-2Ca-Al_2O_3	EISA-one-pot	0.15	0.200	$1.02 \cdot 10^{-5}$	[61]

(e) 20Ni-Al_2O_3	IWI[b]	0.15	1.000	$6.14 \cdot 10^{-6}$	[11]
(f) 9Ni-ZrO_2	IWI[b]	0.16	0.050	$5.46 \cdot 10^{-6}$	[62]
(g) 6Ni-1Mg-ZrO_2	Citrate complexing	0.16	0.200	$5.46 \cdot 10^{-6}$	[63]
(h) 5Ni/CeO_2	Wet impregnation	0.10	0.050	$1.36 \cdot 10^{-6}$	[64]
(i) 10Ni/CeO_2-ZrO_2	NH_3 evaporation	0.08	0.150	$2.73 \cdot 10^{-6}$	[65]
(j) 16Ni/γ-Al_2O_3-ZrO_2-TiO_2-CeO_2	Impregnation	0.03	0.600	$5.12 \cdot 10^{-6}$	[66]
(k) Sponge Ni	Commercial	0.10	0.300	$9.17 \cdot 10^{-6}$	[67]

a: Numbers in the formulation refer to the elemental wt.%
b: Incipient Wetness Impregnation
c: CO_2 partial pressure;
d: Mass of catalyst used per test;
e: Inlet molar flow of CO_2.

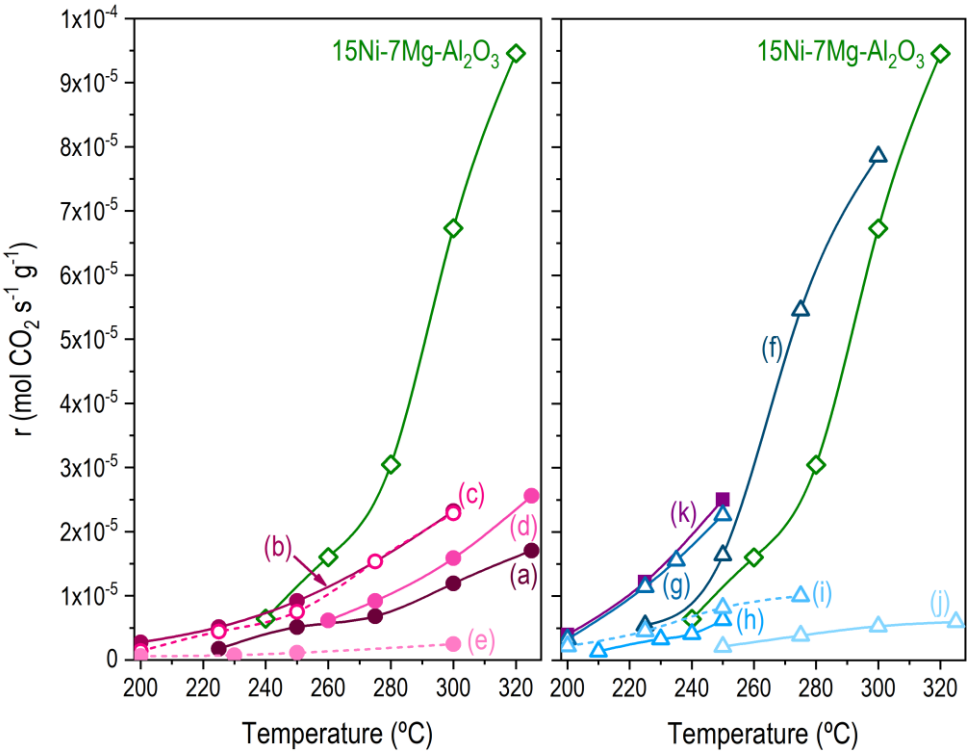

Figure 7. Comparison in the 200-330°C temperature range of the CO_2 conversion rates (in $mol_{CO2}.s^{-1}.g_{cat}^{-1}$) on *15*Ni-*7*Mg-$Al_2O_3$ (present work) and on catalysts of the literature detailed in Table 2: Ni-Al_2O_3 based catalysts (curves (a) to (e)), other Ni-oxides catalysts (curves (f) to (j)) and pure Ni sponge (curve (k)).

4. Conclusion

This work shows firstly that the EISA-one-pot method can be applied successfully to obtain active, selective and stable ordered mesoporous alumina-based catalysts containing varying contents in Ni and Mg well dispersed all over the materials. The increase of the Mg content (0, 7 and 26 wt.%) over 5 wt.% Ni-based systems leads to a stronger interaction between the Ni, Mg and Al species, attested by a shift in the reducibility of the metal species towards higher temperatures. Mg enhances the strength of interaction between water and the material and leads to a loss of mesoporosity when added in too high amount (26 wt.%). In terms of catalytic performances, higher Mg loadings favour both the CO_2 conversion and CH_4 selectivity due to the higher number of Mg sites capable of

activating CO_2. An optimum 7 wt.% Mg based alumina is identified as leading to the best compromise in terms of catalysts properties and catalytic performances. With such Mg content, a variation of the Ni loading from 5 to 10, 15 and finally 20 wt.% does not affect the interaction between the catalysts and water, neither the metal reducibility (high temperature of reduction) that indicates a persistence of a stronger interaction between the Ni and Mg species, even at high Ni content. Additionally, the textural properties are only slightly affected. Hence, increasing the Ni content up to 15 wt.% favours both the conversion of carbon dioxide and the selectivity to methane and this is attributed to the high metallic surface available for the dissociation of hydrogen. The best mesoporous 15Ni-7Mg-Al_2O_3 EISA-one-pot sample obtained shows catalytic performances that are as high as those obtained for a commercial Ni-based alumina hydrogenation catalyst containing a higher (almost double) Ni content (~25 wt.%). The promising activity, selectivity and stability of the prepared materials turn them into potential catalysts for a large-scale application of power-to-gas.

Acknowledgments

The authors are grateful to the FP7 European program and related national organisms for SOL-CARE project funding (ERANETMED_ENERG-065, 2016-2019): the national ANR (France) and CNRS-L (Lebanon). Authors would like to thank the UOBRC for the BIRG 2/2016 and the *Fundação para a Ciência e Tecnologia* (FCT) for the support to the CQE research group (UID/QUI/00100/2019).

References

[1] P. Denholm, E. Ela, B. Kirby, M. Milligan, The Role of energy storage with renewable electricity generation, Publ. E. (2010) 1–61.

[2] T. Weitzel, C.H. Glock, Energy management for stationary electric energy storage systems: A systematic literature review, Eur. J. Oper. Res. 264 (2018) 582–606. https://doi.org/10.1016/j.ejor.2017.06.052.

[3] H. Chen, T.N. Cong, W. Yang, C. Tan, Y. Li, Y. Ding, Progress in electrical energy storage system: A critical review, Prog. Nat. Sci. 19 (2009) 291–312. https://doi.org/10.1016/j.pnsc.2008.07.014.

[4] K. Ghaib, F.-Z. Ben-Fares, Power-to-Methane: A state-of-the-art review, Renew. Sustain. Energy Rev. 81 (2018) 433–446. https://doi.org/10.1016/j.rser.2017.08.004.

[5] P. Riani, G. Garbarino, M.A. Lucchini, F. Canepa, G. Busca, Unsupported versus alumina-supported Ni nanoparticles as catalysts for steam/ethanol conversion and CO2 methanation, J. Mol. Catal. Chem. 383–384 (2014) 10–16. https://doi.org/10.1016/j.molcata.2013.11.006.

[6] G. Garbarino, P. Riani, L. Magistri, G. Busca, A study of the methanation of carbon dioxide on Ni/Al2O3 catalysts at atmospheric pressure, Int. J. Hydrog. Energy. 39 (2014) 11557–11565. https://doi.org/10.1016/j.ijhydene.2014.05.111.

[7] G. Garbarino, D. Bellotti, P. Riani, L. Magistri, G. Busca, Methanation of carbon dioxide on Ru/Al2O3 and Ni/Al2O3 catalysts at atmospheric pressure: Catalysts activation, behaviour and stability, Int. J. Hydrog. Energy. 40 (2015) 9171–9182. https://doi.org/10.1016/j.ijhydene.2015.05.059.
[8] M. a. A. Aziz, A.A. Jalil, S. Triwahyono, A. Ahmad, CO2 methanation over heterogeneous catalysts: recent progress and future prospects, Green Chem. 17 (2015) 2647–2663. https://doi.org/10.1039/C5GC00119F.
[9] X. Guo, A. Traitangwong, M. Hu, C. Zuo, V. Meeyoo, Z. Peng, C. Li, Carbon Dioxide Methanation over Nickel-Based Catalysts Supported on Various Mesoporous Material, Energy Fuels. 32 (2018) 3681–3689. https://doi.org/10.1021/acs.energyfuels.7b03826.
[10] R. Daroughegi, F. Meshkani, M. Rezaei, Enhanced activity of CO2 methanation over mesoporous nanocrystalline Ni-Al2O3 catalysts prepared by ultrasound-assisted co-precipitation method, Int. J. Hydrog. Energy. 42 (2017) 15115–15125. https://doi.org/10.1016/j.ijhydene.2017.04.244.
[11] S. He, C. Li, H. Chen, D. Su, B. Zhang, X. Cao, B. Wang, M. Wei, D.G. Evans, X. Duan, A Surface Defect-Promoted Ni Nanocatalyst with Simultaneously Enhanced Activity and Stability, Chem. Mater. 25 (2013) 1040–1046. https://doi.org/10.1021/cm303517z.
[12] F. Song, Q. Zhong, Y. Yu, M. Shi, Y. Wu, J. Hu, Y. Song, Obtaining well-dispersed Ni/Al2O3 catalyst for CO2 methanation with a microwave-assisted method, Int. J. Hydrog. Energy. 42 (2017) 4174–4183. https://doi.org/10.1016/j.ijhydene.2016.10.141.
[13] X. Shang, D. Deng, X. Wang, X. Zou, W. Ding, X. Lu, Low Temperature Synthesis of Mesoporous gamma-Alumina supported Nickel Oxides and their Catalytic Application for CO2 Methanation, in: Y. He (Ed.), Proc. 2015 Int. Symp. Energy Sci. Chem. Eng. Isesce 2015, Atlantis Press, Paris, 2016: pp. 117–123.
[14] T.A. Le, T.W. Kim, S.H. Lee, E.D. Park, CO and CO2 methanation over Ni catalysts supported on alumina with different crystalline phases, Korean J. Chem. Eng. 34 (2017) 3085–3091. https://doi.org/10.1007/s11814-017-0257-0.
[15] B. Mutz, A.M. Gänzler, M. Nachtegaal, O. Müller, R. Frahm, W. Kleist, J.-D. Grunwaldt, Surface Oxidation of Supported Ni Particles and Its Impact on the Catalytic Performance during Dynamically Operated Methanation of CO2, Catalysts. 7 (2017) 279. https://doi.org/10.3390/catal7090279.
[16] A. Aljishi, G. Veilleux, J.A.H. Lalinde, J. Kopyscinski, The effect of synthesis parameters on ordered mesoporous nickel alumina catalyst for CO2 methanation, Appl. Catal. Gen. 549 (2018) 263–272. https://doi.org/10.1016/j.apcata.2017.10.012.
[17] L. Xu, F. Wang, M. Chen, J. Zhang, K. Yuan, L. Wang, K. Wu, G. Xu, W. Chen, CO2 methanation over a Ni based ordered mesoporous catalyst for the production of synthetic natural gas, RSC Adv. 6 (2016) 28489–28499. https://doi.org/10.1039/C6RA01139J.
[18] L. Karam, J. Reboul, N. El Hassan, J. Nelayah, P. Massiani, Nanostructured Nickel Aluminate as a Key Intermediate for the Production of Highly Dispersed and Stable Nickel Nanoparticles Supported within Mesoporous Alumina for Dry Reforming of Methane, Molecules. 24 (2019). https://doi.org/10.3390/molecules24224107.
[19] K. Jabbour, P. Massiani, A. Davidson, S. Casale, N. El Hassan, Ordered mesoporous “one-pot” synthesized Ni-Mg(Ca)-Al2O3 as effective and remarkably stable catalysts for combined steam and dry reforming of methane (CSDRM), Appl. Catal. B Environ. 201 (2017) 527–542. https://doi.org/10.1016/j.apcatb.2016.08.009.
[20] Q. Liu, B. Bian, J. Fan, J. Yang, Cobalt doped Ni based ordered mesoporous catalysts for CO2 methanation with enhanced catalytic performance, Int. J. Hydrog. Energy. 43 (2018) 4893–4901. https://doi.org/10.1016/j.ijhydene.2018.01.132.
[21] L. Xu, H. Yang, M. Chen, F. Wang, D. Nie, L. Qi, X. Lian, H. Chen, M. Wu, CO2 methanation over Ca doped ordered mesoporous Ni-Al composite oxide catalysts: The promoting effect of basic modifier, J. CO2 Util. 21 (2017) 200–210. https://doi.org/10.1016/j.jcou.2017.07.014.
[22] L. Xu, F. Wang, M. Chen, D. Nie, X. Lian, Z. Lu, H. Chen, K. Zhang, P. Ge, CO2 methanation over rare earth doped Ni based mesoporous catalysts with intensified low-temperature activity, Int. J. Hydrog. Energy. 42 (2017) 15523–15539. https://doi.org/10.1016/j.ijhydene.2017.05.027.

[23] W.A. Wan Abu Bakar, R. Ali, N.S. Mohammad, The effect of noble metals on catalytic methanation reaction over supported Mn/Ni oxide based catalysts, Arab. J. Chem. 8 (2015) 632–643. https://doi.org/10.1016/j.arabjc.2013.06.009.
[24] W. Yang, Y. Feng, W. Chu, Promotion Effect of CaO Modification on Mesoporous Al2O3-Supported Ni Catalysts for CO2 Methanation, Int. J. Chem. Eng. (2016) 2041821. https://doi.org/10.1155/2016/2041821.
[25] C. Liang, X. Hu, T. Wei, P. Jia, Z. Zhang, D. Dong, S. Zhang, Q. Liu, G. Hu, Methanation of CO2 over Ni/Al2O3 modified with alkaline earth metals: Impacts of oxygen vacancies on catalytic activity, Int. J. Hydrog. Energy. 44 (2019) 8197–8213. https://doi.org/10.1016/j.ijhydene.2019.02.014.
[26] G. Garbarino, C. Wang, T. Cavattoni, E. Finocchio, P. Riani, M. Flytzani-Stephanopoulos, G. Busca, A study of Ni/La-Al2O3 catalysts: A competitive system for CO2 methanation, Appl. Catal. B Environ. 248 (2019) 286–297. https://doi.org/10.1016/j.apcatb.2018.12.063.
[27] J.-N. Park, E.W. McFarland, A highly dispersed Pd–Mg/SiO2 catalyst active for methanation of CO2, J. Catal. 266 (2009) 92–97. https://doi.org/10.1016/j.jcat.2009.05.018.
[28] M. Guo, G. Lu, The effect of impregnation strategy on structural characters and CO2 methanation properties over MgO modified Ni/SiO2 catalysts, Catal. Commun. 54 (2014) 55–60. https://doi.org/10.1016/j.catcom.2014.05.022.
[29] X. Li, Y. Wang, G. Zhang, W. Sun, Y. Bai, L. Zheng, X. Han, L. Wu, Influence of Mg-promoted Ni-based Catalyst Supported on Coconut Shell Carbon for CO2 Methanation, ChemistrySelect. 4 (2019) 838–845. https://doi.org/10.1002/slct.201803369.
[30] H.J. Kim, E.H. Yang, Y.S. Noh, G.H. Hong, J.I. Park, S.A. Shin, K.Y. Lee, D.J. Moon, Studies on the steam CO2 reforming of methane over ordered mesoporous nickel–magnesium–alumina catalysts, Res. Chem. Intermed. (2017) 1–18. https://doi.org/10.1007/s11164-017-3156-4.
[31] T. Margossian, K. Larmier, S.M. Kim, F. Krumeich, A. Fedorov, P. Chen, C.R. Müller, C. Copéret, Molecularly Tailored Nickel Precursor and Support Yield a Stable Methane Dry Reforming Catalyst with Superior Metal Utilization, J. Am. Chem. Soc. 139 (2017) 6919–6927. https://doi.org/10.1021/jacs.7b01625.
[32] M.C. Bacariza, I. Graça, S.S. Bebiano, J.M. Lopes, C. Henriques, Micro- and mesoporous supports for CO2 methanation catalysts: A comparison between SBA-15, MCM-41 and USY zeolite, Chem. Eng. Sci. 175 (2018) 72–83. https://doi.org/10.1016/j.ces.2017.09.027.
[33] S.M. Morris, P.F. Fulvio, M. Jaroniec, Ordered mesoporous alumina-supported metal oxides, J. Am. Chem. Soc. 130 (2008) 15210–15216. https://doi.org/10.1021/ja806429q.
[34] L. Karam, N. El Hassan, Advantages of mesoporous silica based catalysts in methane reforming by CO2 from kinetic perspective, J. Environ. Chem. Eng. 6 (2018) 4289–4297. https://doi.org/10.1016/j.jece.2018.06.031.
[35] L. Karam, S. Casale, H. El Zakhem, N. El Hassan, Tuning the properties of nickel nanoparticles inside SBA-15 mesopores for enhanced stability in methane reforming, J. CO2 Util. 17 (2017) 119–124. https://doi.org/10.1016/j.jcou.2016.12.002.
[36] I. Graça, L.V. González, M.C. Bacariza, A. Fernandes, C. Henriques, J.M. Lopes, M.F. Ribeiro, CO2 hydrogenation into CH4 on NiHNaUSY zeolites, Appl. Catal. B Environ. 147 (2014) 101–110. https://doi.org/10.1016/j.apcatb.2013.08.010.
[37] M.C. Bacariza, I. Graça, A. Westermann, M.F. Ribeiro, J.M. Lopes, C. Henriques, CO2 Hydrogenation Over Ni-Based Zeolites: Effect of Catalysts Preparation and Pre-reduction Conditions on Methanation Performance, Top. Catal. 59 (2015) 314–325. https://doi.org/10.1007/s11244-015-0435-4.
[38] M.W. Anderson, J. Klinowski, Zeolites treated with silicon tetrachloride vapour. Part 1.—Preparation and characterisation, J. Chem. Soc. Faraday Trans. 1 Phys. Chem. Condens. Phases. 82 (1986) 1449–1469. https://doi.org/10.1039/F19868201449.
[39] M. Thommes, K. Kaneko, A.V. Neimark, J.P. Olivier, F. Rodriguez-Reinoso, J. Rouquerol, K.S.W. Sing, Physisorption of gases, with special reference to the evaluation of surface area and pore size distribution (IUPAC Technical Report), Pure Appl. Chem. 87 (2015) 1051–1069. https://doi.org/10.1515/pac-2014-1117.

[40] D. Pan, Z. Dong, M. He, W. Chen, S. Chen, F. Yu, B. Fan, X. Cui, R. Li, Structural and surface properties of highly ordered mesoporous magnesium-aluminium composite oxides derived from facile synthesis, Mater. Chem. Phys. 186 (2017) 574–583. https://doi.org/10.1016/j.matchemphys.2016.11.038.
[41] Z. Zhang, Y. Tian, L. Zhang, S. Hu, J. Xiang, Y. Wang, L. Xu, Q. Liu, S. Zhang, X. Hu, Impacts of nickel loading on properties, catalytic behaviors of Ni/γ–Al2O3 catalysts and the reaction intermediates formed in methanation of CO2, Int. J. Hydrog. Energy. 44 (2019) 9291–9306. https://doi.org/10.1016/j.ijhydene.2019.02.129.
[42] V. Chaudhary, S. Sharma, An overview of ordered mesoporous material SBA-15: synthesis, functionalization and application in oxidation reactions, J. Porous Mater. 24 (2017) 741–749. https://doi.org/10.1007/s10934-016-0311-z.
[43] M.A.A. Aziz, A.A. Jalil, S. Triwahyono, M.W.A. Saad, CO2 methanation over Ni-promoted mesostructured silica nanoparticles: Influence of Ni loading and water vapor on activity and response surface methodology studies, Chem. Eng. J. 260 (2015) 757–764. https://doi.org/10.1016/j.cej.2014.09.031.
[44] R. Delmelle, R.B. Duarte, T. Franken, D. Burnat, L. Holzer, A. Borgschulte, A. Heel, Development of improved nickel catalysts for sorption enhanced CO2 methanation, Int. J. Hydrog. Energy. 41 (2016) 20185–20191. https://doi.org/10.1016/j.ijhydene.2016.09.045.
[45] M.C. Bacariza, R. Bértolo, I. Graça, J.M. Lopes, C. Henriques, The effect of the compensating cation on the catalytic performances of Ni/USY zeolites towards CO2 methanation, J. CO2 Util. 21 (2017) 280–291. https://doi.org/10.1016/j.jcou.2017.07.020.
[46] L. Karam, J. Reboul, S. Casale, P. Massiani, N.E. Hassan, Porous Nickel-Alumina Derived from Metal-Organic Framework (MIL-53): A New Approach to Achieve Active and Stable Catalysts in Methane Dry Reforming, ChemCatChem. 12 (2020) 373–385. https://doi.org/10.1002/cctc.201901278.
[47] D. Hu, J. Gao, Y. Ping, L. Jia, P. Gunawan, Z. Zhong, G. Xu, F. Gu, F. Su, Enhanced Investigation of CO Methanation over Ni/Al2O3 Catalysts for Synthetic Natural Gas Production, Ind. Eng. Chem. Res. 51 (2012) 4875–4886. https://doi.org/10.1021/ie300049f.
[48] M.C. Bacariza, I. Graça, S.S. Bebiano, J.M. Lopes, C. Henriques, Magnesium as Promoter of CO2 Methanation on Ni-Based USY Zeolites, Energy Fuels. 31 (2017) 9776–9789. https://doi.org/10.1021/acs.energyfuels.7b01553.
[49] J. Guo, H. Lou, H. Zhao, X. Zheng, Improvement of stability of out-layer MgAl2O4 spinel for a Ni/MgAl2O4/Al2O3 catalyst in dry reforming of methane, React. Kinet. Catal. Lett. 84 (2005) 93–100. https://doi.org/10.1007/s11144-005-0195-4.
[50] H. Liu, H. Wang, J. Shen, Y. Sun, Z. Liu, Preparation, characterization and activities of the nano-sized Ni/SBA-15 catalyst for producing COx-free hydrogen from ammonia, Appl. Catal. Gen. 337 (2008) 138–147. https://doi.org/10.1016/j.apcata.2007.12.006.
[51] A. Quindimil, U. De-La-Torre, B. Pereda, J.A. González-Marcos, J.R. González-Velasco, Ni catalysts with La as promoter supported over Y- and Beta- zeolites for CO2 methanation, Appl. Catal. B Environ. 238 (2018) 393–403. https://doi.org/10.1016/j.apcatb.2018.07.034.
[52] Goodarzi Farnoosh, Kang Liqun, Wang Feng Ryan, Joensen Finn, Kegnæs Søren, Mielby Jerrik, Methanation of Carbon Dioxide over Zeolite-Encapsulated Nickel Nanoparticles, ChemCatChem. 10 (2018) 1566–1570. https://doi.org/10.1002/cctc.201701946.
[53] Collection of Simulated XRD Powder Patterns for Zeolites, Elsevier, 2007. https://doi.org/10.1016/B978-0-444-53067-7.X5470-7.
[54] H.Y. Kim, H.M. Lee, J.-N. Park, Bifunctional Mechanism of CO2 Methanation on Pd-MgO/SiO2 Catalyst: Independent Roles of MgO and Pd on CO2 Methanation, J. Phys. Chem. C. 114 (2010) 7128–7131. https://doi.org/10.1021/jp100938v.
[55] A. Cárdenas-Arenas, A. Quindimil, A. Davó-Quiñonero, E. Bailón-García, D. Lozano-Castelló, U. De-La-Torre, B. Pereda-Ayo, J.A. González-Marcos, J.R. González-Velasco, A. Bueno-López, Isotopic and in situ DRIFTS study of the CO2 methanation mechanism using Ni/CeO2 and Ni/Al2O3 catalysts, Appl. Catal. B Environ. 265 (2020) 118538. https://doi.org/10.1016/j.apcatb.2019.118538.

[56] A. Westermann, B. Azambre, M.C. Bacariza, I. Graça, M.F. Ribeiro, J.M. Lopes, C. Henriques, Insight into CO2 methanation mechanism over NiUSY zeolites: An operando IR study, Appl. Catal. B Environ. 174–175 (2015) 120–125. https://doi.org/10.1016/j.apcatb.2015.02.026.
[57] H.C. Wu, Y.C. Chang, J.H. Wu, J.H. Lin, I.K. Lin, C.S. Chen, Methanation of CO2 and reverse water gas shift reactions on Ni/SiO2 catalysts: the influence of particle size on selectivity and reaction pathway, Catal. Sci. Technol. 5 (2015) 4154–4163. https://doi.org/10.1039/c5cy00667h.
[58] K. Zhao, W. Wang, Z. Li, Highly efficient Ni/ZrO2 catalysts prepared via combustion method for CO2 methanation, J. Co2 Util. 16 (2016) 236–244. https://doi.org/10.1016/j.jcou.2016.07.010.
[59] G. Du, S. Lim, Y. Yang, C. Wang, L. Pfefferle, G.L. Haller, Methanation of carbon dioxide on Ni-incorporated MCM-41 catalysts: The influence of catalyst pretreatment and study of steady-state reaction, J. Catal. 249 (2007) 370–379. https://doi.org/10.1016/j.jcat.2007.03.029.
[60] P.A.U. Aldana, F. Ocampo, K. Kobl, B. Louis, F. Thibault-Starzyk, M. Daturi, P. Bazin, S. Thomas, A.C. Roger, Catalytic CO2 valorization into CH4 on Ni-based ceria-zirconia. Reaction mechanism by operando IR spectroscopy, Catal. Today. 215 (2013) 201–207. https://doi.org/10.1016/j.cattod.2013.02.019.
[61] Q. Liu, S. Wang, G. Zhao, H. Yang, M. Yuan, X. An, H. Zhou, Y. Qiao, Y. Tian, CO2 methanation over ordered mesoporous NiRu-doped CaO-Al2O3 nanocomposites with enhanced catalytic performance, Int. J. Hydrog. Energy. 43 (2018) 239–250. https://doi.org/10.1016/j.ijhydene.2017.11.052.
[62] X. Jia, X. Zhang, N. Rui, X. Hu, C. Liu, Structural effect of Ni/ZrO2 catalyst on CO2 methanation with enhanced activity, Appl. Catal. B Environ. 244 (2019) 159–169. https://doi.org/10.1016/j.apcatb.2018.11.024.
[63] J. Tan, J. Wang, Z. Zhang, Z. Ma, L. Wang, Y. Liu, Highly dispersed and stable Ni nanoparticles confined by MgO on ZrO2 for CO2 methanation, Appl. Surf. Sci. 481 (2019) 1538–1548. https://doi.org/10.1016/j.apsusc.2019.03.217.
[64] Z. Bian, Y.M. Chan, Y. Yu, S. Kawi, Morphology dependence of catalytic properties of Ni/CeO2 for CO2 methanation: A kinetic and mechanism study, Catal. Today. 347 (2020) 31–38. https://doi.org/10.1016/j.cattod.2018.04.067.
[65] J. Ashok, M.L. Ang, S. Kawi, Enhanced activity of CO2 methanation over Ni/CeO2-ZrO2 catalysts: Influence of preparation methods, Catal. Today. 281 (2017) 304–311. https://doi.org/10.1016/j.cattod.2016.07.020.
[66] S. Abate, C. Mebrahtu, E. Giglio, F. Deorsola, S. Bensaid, S. Perathoner, R. Pirone, G. Centi, Catalytic Performance of gamma-Al2O3-ZrO2-TiO2-CeO2 Composite Oxide Supported Ni-Based Catalysts for CO2 Methanation, Ind. Eng. Chem. Res. 55 (2016) 4451–4460. https://doi.org/10.1021/acs.iecr.6b00134.
[67] S. Tada, S. Ikeda, N. Shimoda, T. Honma, M. Takahashi, A. Nariyuki, S. Satokawa, Sponge Ni catalyst with high activity in CO2 methanation, Int. J. Hydrog. Energy. 42 (2017) 30126–30134. https://doi.org/10.1016/j.ijhydene.2017.10.138.